Tolerance of Al–Mg–Si Wrought Alloys for High Fe Contents: The Role of Effective Si

J.A. ÖSTERREICHER [ID], A.R. ARNOLDT, S. GNEIGER, and G. KUNSCHERT

Aluminum scrap is often contaminated with steel parts, leading to accumulation of Fe in recycled Al alloys. Consequently, low limits for Fe in Al wrought alloys are difficult to meet by recycling without dilution with primary Al. Wrought alloys with a higher tolerance for Fe could help overcome this problem and improve the sustainability of Al wrought products. Here we study the effects of increasing the Fe content in EN AW-6060, 6005A, and 6082 from 0.2 to 0.7 wt pct. The microstructure and mechanical properties of the alloys after extrusion and artificial ageing are compared to the standard alloys. We found that 6082 is more tolerant to above-standard Fe contents than 6005A, which in turn is more tolerant than 6060: the strength of the 6082-based alloy with increased Fe content is comparable to that of standard 6082 and the elongation at break is increased. In contrast, the artificial ageing potential of the 6060-based alloy with more Fe is drastically reduced compared to 6060. This data and literature values show that the effective Si content is a good overall predictor of alloy strength. Effective Si is not bound in AlFeSi-type phases and is available for precipitation hardening. Additional effects of increased Fe levels are discussed.

I. INTRODUCTION

GENERALLY, high iron levels are undesirable in Al–Mg–Si wrought alloys because Fe forms brittle intermetallic phases with Al and Si. These AlFeSi-type intermetallics are known fracture initiation sites and thought to reduce ductility and formability.[1–3] In the extrusion process, AlFeSi-type intermetallics can lead to inferior surface finish.[4,5] Common stoichiometries of the intermetallics are $Al_{12}(Fe, Mn, Cr)_3Si_{1-2}$ (α-type) and Al_5FeSi (β-type).[6] Because the solubility of Fe in a solid Al matrix is extremely low even at elevated temperatures,[7] the vast majority of Fe atoms of an Fe-containing Al alloy are found in the intermetallics, leading to a corresponding reduction of Si in the matrix. The AlFeSi-type intermetallics are very stable and do not dissolve during solution heat treatment. Consequently, for a given Si content, rising amounts of Fe decrease the amount of Si that can be dissolved in the matrix and thus is available for subsequent artificial ageing. This silicon not bound in the AlFeSi-type intermetallics is known as *effective silicon*.[8,9] To mitigate the loss of Si and ensure an adequate level of effective Si, additional alloying can be employed,[10–12] but the potential possible negative effects of AlFeSi-phases persist.

Unfortunately, aluminum scrap is often contaminated with steel parts. Additionally, steel tools are widely used in the handling of Al melts and products, posing another source of Fe contamination. Since Fe is difficult to remove metallurgically from Al melts, dilution with high-purity primary Al is the standard procedure to meet the rather low maximum permissible Fe levels imposed by standard wrought alloy compositions (*cf.* DIN EN 573-3:2009). Typically, more than 50 pct of primary Al must be added, even for wrought alloys with relatively high Fe limits.[13]

Recycling of Al requires only 5 to 10 pct of the energy needed for primary production; additionally, environmental problems related to bauxite extraction and red mud disposal are avoided. In light of the climate crisis and the destruction of natural habitats, improving the sustainability of Al products by increasing their recycled contents is of great importance. In particular, it is desirable to avoid down-cycling of wrought alloys into cast alloys. To achieve these goals, the development of wrought alloys with increased tolerance for tramp elements, most importantly Fe, is key. However, research on the tolerance of wrought alloys to elevated Fe levels is scarce because previously, scrap with increased Fe levels was used mainly for cast alloys.[13]

J.A. ÖSTERREICHER, A.R. ARNOLDT, S. GNEIGER, and G. KUNSCHERT are with the LKR Light Metals Technologies, Austrian Institute of Technology, Lamprechtshausenerstr. 61, Ranshofen 5282, Austria. Contact e-mail: johannes.oesterreicher@ait.ac.at

In the following, several studies that contain variation of Fe content of Al–Mg–Si alloys and that report tensile properties are summarized: Sarkar et al.[1] studied 6111-T4 with high (0.68 wt pct) and low (0.06 wt pct) Fe levels and found little influence on tensile properties but reduced bendability. The high-Fe alloy had finer grain but showed considerably larger dimples in fracture surfaces. Kato et al.[14] found slightly increasing ultimate tensile strength (UTS) and strongly improved elongation at break with increasing Fe content (up to 0.5 wt pct) in Al–Mg–Si extrusion alloys despite not compensating for effective Si loss due to formation of AlFeSi-type intermetallics (the Si content was fixed to 1 wt pct). Furthermore, the variation of Cu and Si contents was studied. Zhao et al.[10] found that the addition of 0.2 wt pct Fe to a lean Al–0.5Mg–0.35Si (wt pct) alloy, then falling within the limits of EN AW-6060 (requiring 0.1 wt pct Fe), increases conductivity but reduces strength; the decrease in strength could be compensated for by increasing the Si content to 0.5 wt pct. Wang et al.[11] designed two alloys, based on EN AW-6082, with increased Fe, Mn, Mg and Si contents; they reported increased strength and only slight or insignificant decrease in elongation in the rolled material. In a recent study, Trink et al.[12] report excellent mechanical properties in a rolling alloy based on EN AW-6016 with drastically increased Fe and Si contents. Additionally, significantly smaller grains and higher strain hardening compared to the reference EN AW-6016 were reported. Trink et al. suggest that wrought alloys with Fe contents significantly exceeding those of current standards have great potential.

In this study, we investigate Al–Mg–Si wrought alloys, based on common extrusion alloys, with high, non-standard Fe contents (i.e., 0.7 wt pct). The mechanical properties of the alloys after extrusion and artificial ageing are reported. In contrast to other studies, the Si content was not increased to compensate for loss of effective Si by formation of AlFeSi-type intermetallics. Thus, the robustness of the alloys for varying Fe contents without further variation could be studied—in view of the potentially changing Fe content of industrial scrap streams.

II. ALLOY DESIGN

Al–Mg–Si alloys EN AW-6060, EN AW-6005A, and EN AW-6082 were selected for this study because they are common extrusion alloys for applications requiring low (6060), medium (6005A), or high strength (6082). The Mg and Si levels were chosen to be the mean of the respective alloy limits, see Figure 1(a). Regions where the alloy definitions overlap were thus avoided. For the other elements except Fe, the same approach was chosen; the alloy compositions are given in Table I. The Fe content was chosen as 0.2 wt pct.

Based on these three alloys, three non-standard alloys with an increased Fe level of 0.7 wt pct were designed, designated as 6060 + Fe, 6005A + Fe, and 6082 + Fe, also given in Table I. Besides Mg, Si, and Fe levels, the

Mn content is the largest difference between the alloys. Mn can substitute Fe in the α-Al_{12}(Fe, Mn, Cr)$_3Si_{1-2}$-phase and thus also binds Si; therefore, Mn and Fe levels together with the alloys' limits are given in Figure 1(b). Mn contents of our alloys were again chosen to be in the middle of the respective limits, Fe levels of 0.2 wt pct are also close to the mean value of permitted values, but Fe levels of 0.7 wt pct are out of the specification for all alloys.

III. METHODS

Round billets with dimensions of 65 mm in diameter and 230 mm in length were gravity die cast. Optical emission spectroscopy with a Spectro Spectromaxx 6 confirmed the alloy compositions, meeting desired contents (Table I) within ± 0.05 wt pct tolerance. The billets were machined to 58.5 mm in diameter and 180 mm in length and homogenized at 580 °C (6082, 6082 + Fe) or 540 °C (other alloys). The heating rate was 180 K/h, soak time was 4 hours, and the cooling rate (forced air) was 800 K/h.[15]

The billets were extruded into "ruler" profiles with a Müller Engineering 1.5 MN extrusion plant. The extrusion ratio was 1:48, the geometry is given in Figure 2. Billets were pre-heated inductively to 490 °C, the container and die temperatures were also set to 490 °C. Profiles were extruded at ram speeds of 1, 2, and 4 mm/s.

Solution heat treatment (SHT) was performed at 560 °C (6082, 6082 + Fe) or 540 °C (other alloys) for 30 min (time in furnace) and quenched in water. The SHT temperatures were chosen to ensure total dissolution of Mg_2Si based on calculation of phase diagrams (CALPHAD) equilibrium phase fraction calculations, given in the Supplementary Materials. Details on CALPHAD calculation methods are given below. After SHT and quenching, the profiles were artificially aged at 180 °C for 8 hours[16] without significant prior storage at room temperature.

Tensile specimens according to DIN 50125 (gauge length $L_0 = 20$ mm, reduced section length $L_c = 26$ mm, reduced section width $b_0 = 6$ mm) were machined in extrusion direction from the center section of the profile. Tensile testing on a Zwick Z250 tensile testing machine was performed according to ÖNORM EN ISO 6892-1B.

Sections for microscopic investigation were produced using standard metallographic techniques, with Struers OP-S 0.25 μm colloidal silica suspension as the final polishing step. Scanning electron microscopy (SEM) was performed using a Tescan Mira 3 microscope operated at 20 kV. A four-quadrant solid-state backscattered electron (BSE) detector was used for imaging of polished sections. For fracture surfaces, the combined signal of the BSE detector and an Everhart–Thornley secondary electron (SE) was used. Energy-dispersive X-ray spectroscopy (EDS) point spectra of intermetallic phases were acquired using a EDAX Octane Elect 70 mm^2 EDS detector. Additionally, an Olympus BX60M light microscope was used. The area
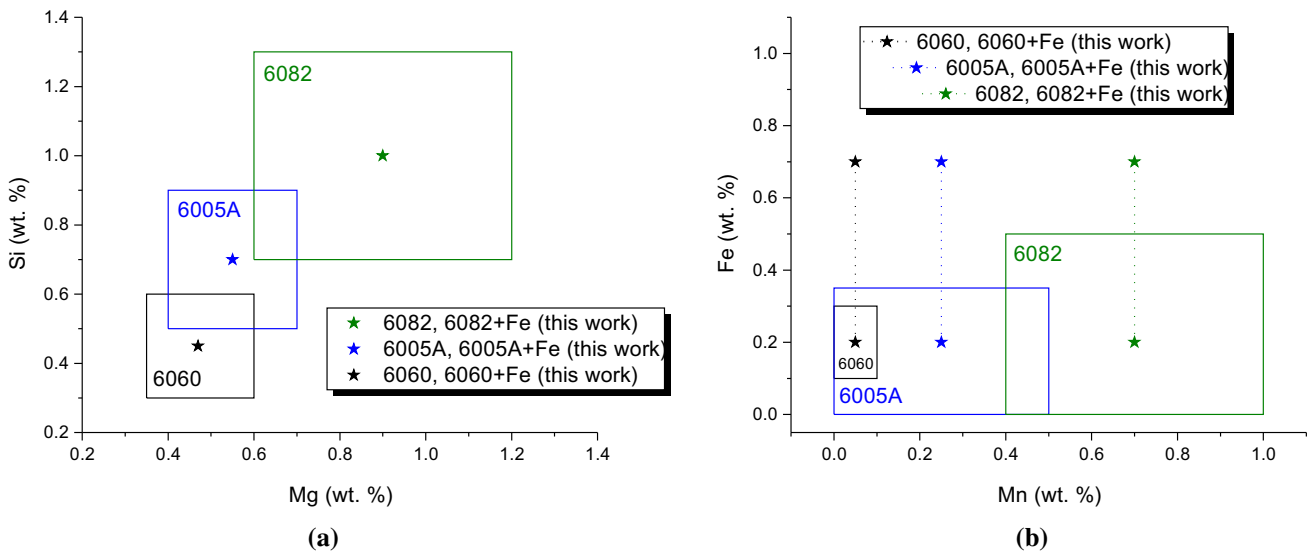
Fig. 1—Standard Mg, Si (*a*) and Mn, Fe (*b*) levels of aluminum alloys 6060, 6005A, and 6082, outlined as squares. The compositions used in this work are marked with stars.

Table I. Alloy Compositions Used in This Work (Wt Pct, Remainder: Al)

Alloy	Si	Mg	Cu	Mn	Fe	Zn	Cr	Ti
6060, 6060 + Fe	0.45	0.47	0.05	0.05	0.2/0.7	0.07	0.05	0.05
6005A, 6005A + Fe	0.7	0.55	0.15	0.25	0.2/0.7	0.10	0.15	0.05
6082, 6082 + Fe	1.0	0.90	0.05	0.70	0.2/0.7	0.10	0.12	0.05
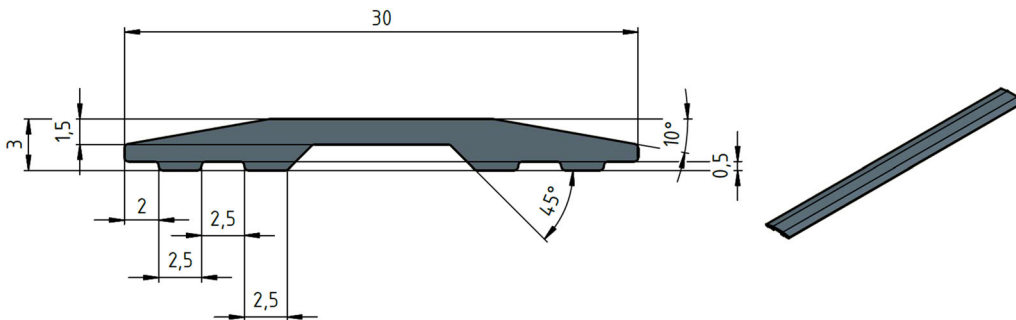
Fig. 2—"Ruler" profile cross-section geometry (left) and isometric drawing (right).

fraction of intermetallic phases was obtained by thresholding from several optical micrographs.

CALPHAD calculations of equilibrium phase fractions and of element ratios in intermetallic phases at SHT temperature were carried out using Thermo-Calc 6 2022a software with the ThermoTech TTAl8.1 database.

IV. RESULTS AND DISCUSSION

The microstructure of the alloys in the as-cast state and after extrusion is given in Figure 3. In the as-cast state, coarse Mg_2Si phase particles are visible, which appear black in the optical micrographs. As to be expected, higher Fe levels increase the amount of AlFeSi-type intermetallic phases. The increased amount of AlFeSi-type particles precipitates predominantly in a fine, Chinese script-type morphology in alloys 6005A, 6082, and their variations with increased Fe. This morphology is a hallmark of α-type AlFeSi such as $Al_{12}(Fe, Mn, Cr)_3Si_{1-2}$, which is less detrimental to extrudability and mechanical properties than the β-type (Al_5FeSi) due to its more rounded shape.[6,17] The formation of α-type AlFeSi already in the as-cast state is favored by higher contents of Mn. Additional β to α transformation takes place during homogenization, also facilitated by Mn.[6] In contrast, 6060 and, especially, 6060 + Fe exhibit also many large needle-shaped particles in the as-cast state, likely β-Al_5FeSi, in addition to the phase with Chinese script morphology. The presence
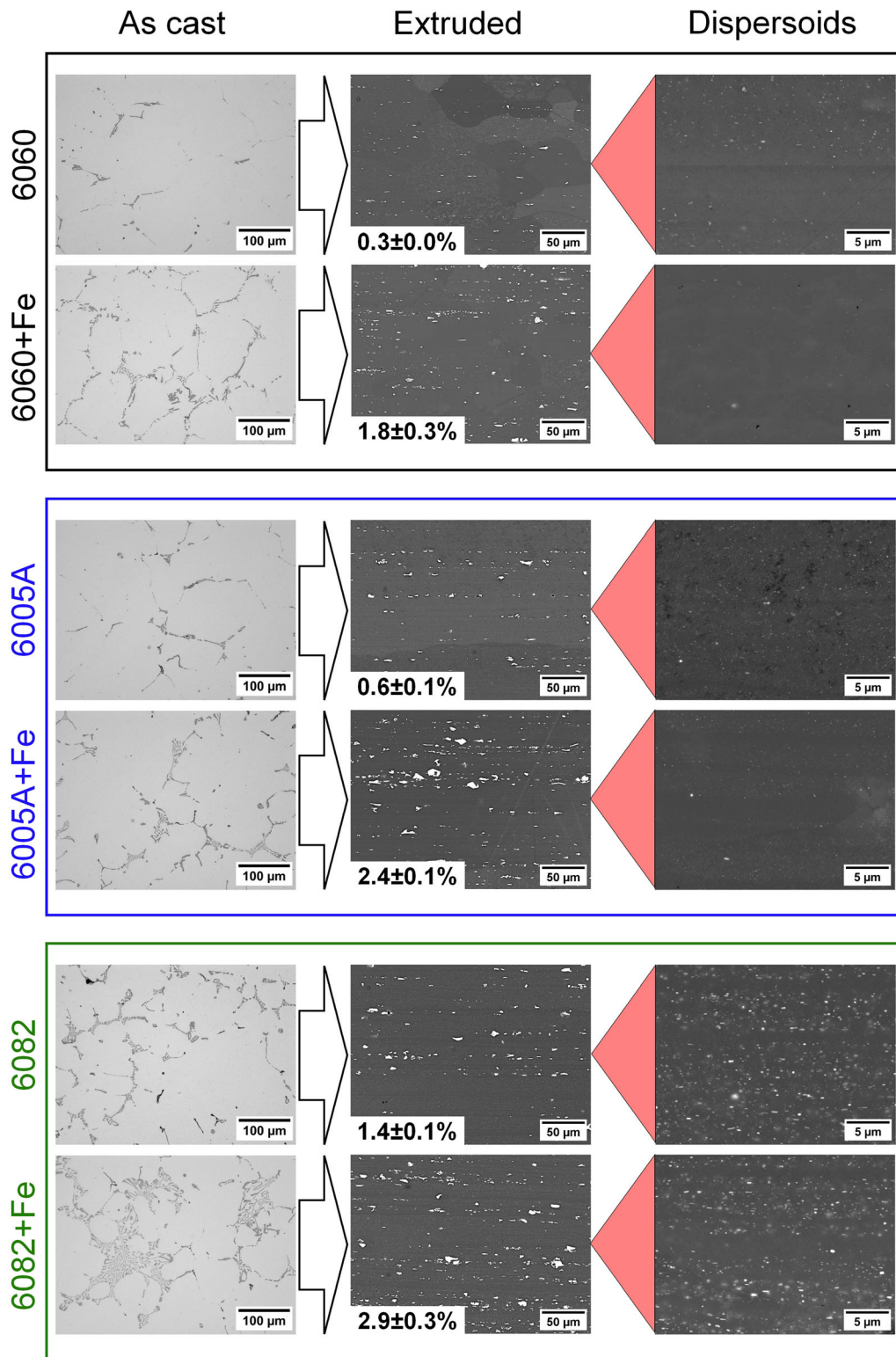
Fig. 3—Microstructure of the as-cast and extruded states (optical and BSE micrographs).

of β-Al$_5$FeSi can be explained by the low Mn content of 6060 and 6060 + Fe.

During extrusion, the AlFeSi-type intermetallics are broken up into smaller fragments and aligned in rows in extrusion direction. The area fraction of intermetallic phases (obtained from several light micrographs, not shown here) is given as inset percentage number in Figure 3. The amount of intermetallic phases correlates with Fe + Mn content. Intragranularly, nanoscale dispersoids are visible. While the distribution of
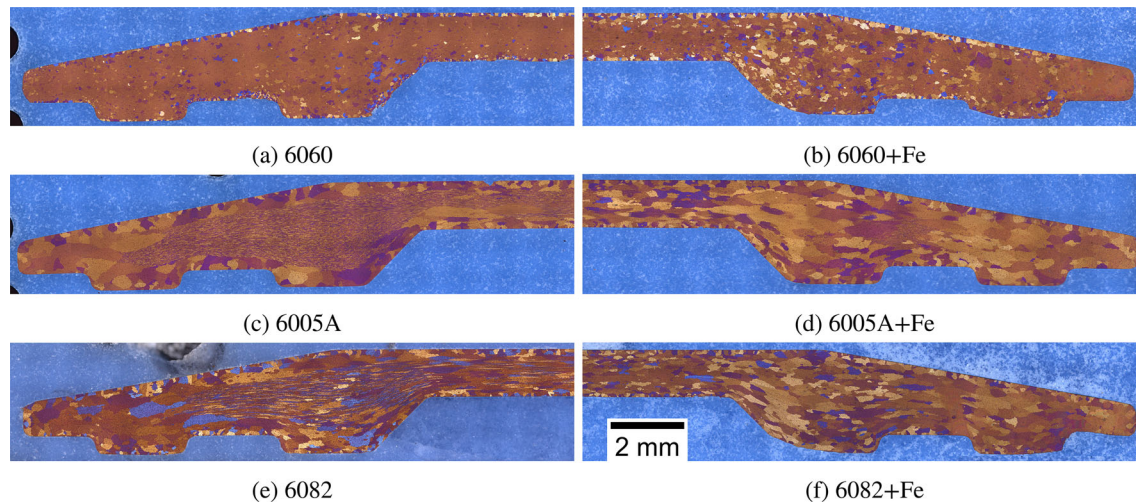
(a) 6060

(b) 6060+Fe

(c) 6005A

(d) 6005A+Fe

(e) 6082

2 mm

(f) 6082+Fe

Fig. 4—Grain structure after extrusion at a ram speed of 2 mm/s. Optical micrographs, Barker's etchant. The scale bar in (*f*) also applies to (*a* through *e*).

dispersoids appears to be slightly altered with increased Fe content, it is difficult to identify a clear trend.

Despite the pinning effect of dispersoids, the profiles with increased Fe content showed stronger recrystallization and grain growth during extrusion, see Figure 4, likely due to particle stimulated nucleation (PSN) caused by coarse AlFeSi-type particles.[18,19]

Grain refinement is an important strengthening mechanism in Al–Mg series (5xxx series), which have a relatively large Hall–Petch coefficient compared with other Al wrought alloys.[20,21] In contrast, the direct influence of grain size on the strength of Al–Mg–Si (6xxx series) alloys is rather small, except for ultra-fine-grained alloys,[22] and the formation of second-phase hardening precipitates is most important.[23] Nevertheless, coarse grain, especially peripheral coarse grain zones, can have a negative impact on formability and crashworthiness, fatigue behavior, visual appearance after anodization, corrosion resistance, *etc*.[24–26] The coarser grain of the high-Fe alloys may thus not be acceptable for all applications.

Let us now consider the tensile properties of the artificially aged profiles. There were no significant difference for different extrusion speeds, thus the values reported in Table II are average values from profiles extruded at the three different speeds (1, 2, and 4 mm/s ram speed). Additionally, Figure 5 gives exemplary tensile curves.

6082 is most robust against increased Fe levels, with 6082 + Fe showing comparable strength to 6082. Both the 6082 and 6082 + Fe alloys easily outperform the minimum requirements for yield strength (YS) and UTS of 250 and 290 MPa, respectively, laid out in EN 755-2 for EN AW-6082-T6 < 5 mm. The elongation at break is significantly increased for 6082 + Fe ($p = 0.02$). The increase in elongation is surprising since AlFeSi-type intermetallics are known fracture initiation sites.[3] Surprisingly high elongation was also reported by Trink et al.,[12] ascribed to the small size and spherical

morphology of the AlFeSi-type particles, the small matrix grain size, and the geometrically necessary dislocation forest surrounding the particles. Kato et al.[14] also found significantly improved elongation values with increasing Fe content and ascribed this to the influence of grain refinement by PSN and other factors, such as prevention of grain boundary embrittlement by Si.

There are a higher number of intermetallic particles in our alloy, roughly double the amount found in 6082, but they appear similar in size (Figure 3). This could help to achieve more uniform deformation.[12] The fracture surfaces are given in Figure 6. Both alloys exhibit large dimples that originate from the fracture of coarse AlFeSi-type particles, as evidenced by the remnants of these particles visible in the center of the dimples. In addition, between the large dimples, there are smaller dimples that are likely caused by the nucleation of voids at dispersoids.[2,3,27] However, the average size of the dimples originating at the coarse AlFeSi-type particles is much smaller in 6082 + Fe (Figure 6(b)). This could be related to the higher number of such particles and the later onset of fracture due to a higher capacity to store deformation, similar to what is described by Trink et al.[12]

6005A is also quite tolerant to elevated Fe levels, yet there is some decrease in YS and UTS in 6005A + Fe. However, 6005 + Fe still fulfills the requirements from EN 755-2 for YS and UTS easily (225 and 270 MPa, respectively) and the elongation at break is comparable to the standard alloy (Table II). Furthermore, 6005A + Fe shows stronger work hardening than 6005A.

In contrast, the strength of 6060 strongly decreases with the increased Fe level, with the YS and UTS of 6060 + Fe resembling those of alloys of the 1xxx series that are incapable of age hardening. The stress/strain curve appears serrated, which can be related to Mg in solid solution (Portevin–Le Chatelier effect). 6060 + Fe clearly misses the limits defined in EN 755-2 for YS and

Table II. Tensile Properties

	YS (MPa)	UTS (MPa)	Uniform Elongation (Pct)	Elongation at Break (Pct)
6060	168 ± 8	194 ± 8	4.2 ± 0.8	9.6 ± 1.4 ($n = 3$)
6060 + Fe	81 ± 5	130 ± 5	7.6 ± 1.3	12.4 ± 1.3
6005A	254 ± 4	264 ± 4	5.3 ± 0.7	10.0 ± 2.1
6005A + Fe	218 ± 9	241 ± 8	5.5 ± 0.5	9.8 ± 1.6
6082	340 ± 4	355 ± 4	5.6 ± 1.4	9.0 ± 1.9
6082 + Fe	331 ± 5	352 ± 5	6.9 ± 0.6	10.7 ± 1.4

Plus–minus values represent standard deviation ($n = 12$, unless otherwise stated).

UTS (150 and 190 MPa, respectively). In view of the low strength, the increased elongation at break is but a small redemption.

In the following, the reasons for the lower strength of Fe-containing alloys are discussed, as well as the apparent higher robustness of the higher-strength alloys to increased Fe levels. The main hardening phase in 6xxx series alloys is β'', the composition of which has been reported to be Mg_5Si_6.[28,29] Later, it has been suggested, based on first principles calculations, that Si can be partly replaced with Al, resulting in a stoichiometry of $Mg_{4+x}Al_{3-x}Si_4$.[30,31] This structure is in better agreement with Mg/Si ratios close to unity or slightly above obtained by atom probe tomography and atom probe field ion microscopy.[30,32] This means that approximately the same number of Si atoms in solid solution after quenching (effective Si) is needed for each Mg atom to achieve optimum age hardening potential. When Mg is not the limiting factor, as is the case in our alloys, effective Si (*i.e.*, the amount of Si not bound in AlFeSi-type particles) determines the age hardening potential. The amount of effective Si in atomic percent can be calculated as follows (cf.[9]):

$$C_{Si}^{eff.} = C_{Si}^0 - \frac{x}{3}\left(C_{Fe}^0 + C_{Mn}^0 + C_{Cr}^0\right), \qquad [1]$$

where C_{El}^0 is the nominal atomic fraction of an element in the alloy. This calculation assumes that all Fe atoms are bound in the α-$Al_{12}(Fe, Mn, Cr)_3Si_x$ phase, which is dominant in many 6xxx series alloys after homogenization,[6] together with a corresponding amount of Si atoms, which are thus no longer available for age hardening. The variable x serves to calculate the fraction of Si atoms in the α-$Al_{12}(Fe, Mn, Cr)_3Si_x$ phase. It has been reported that x ranges from 1 to 2.[17] Other factors than $\frac{x}{3}$ can be used for other AlFeSi-type phases. The solubility of Si in Al at the ageing temperature is below 0.01 at. pct and can be neglected.[33]

To determine x, we measured the $(C_{Fe} + C_{Mn} + C_{Cr}) : C_{Si}$ ratio (where C_{El} are the atomic fractions) in the coarse intermetallic phases present in the alloys after extrusion (Figure 3) using EDS and the results are presented in Figure 7. For comparison, the ratios were calculated using Thermo-Calc software, also given in Figure 7. With the exception of 6060 + Fe, the ratio of our alloys ranges from 1.5 to 2 in both the EDS measurements and the Thermo-Calc predictions, meaning that x is between 2 and 1.5 as well. For 6060 + Fe, $(C_{Fe} + C_{Mn} + C_{Cr}) : C_{Si}$ was measured as 2.9±1.1 and calculated using Thermo-Calc as 2.1. The higher $(C_{Fe} + C_{Mn} + C_{Cr}) : C_{Si}$ ratio may be explained by the high $C_{Fe}^0 : C_{Si}^0$ ratio in the alloy. It is also possible that other AlFeSi-type phases than α-$Al_{12}(Fe, Mn, Cr)_3Si_x$ are present in the alloy, especially given the low Mn content—Mn facilitates the formation of the α-type phase.[6] However, α-$Al_{12}(Fe, Mn, Cr)_3Si_x$ is the equilibrium phase in all alloys according to our Thermo-Calc calculations.

In the following, a $(C_{Fe} + C_{Mn} + C_{Cr}) : C_{Si}$ ratio in the AlFeSi-type phases of 2 will be used for the analysis [or $x = 1.5$ in $Al_{12}(Fe, Mn, Cr)_3Si_x$], as the use of a fixed fraction for all alloys will allow for better comparison with literature data. Other ratios will be considered in the discussion.

Plotting YS against $C_{Si}^{eff.}$ confirms the previous assumption that the strength increases with $C_{Si}^{eff.}$, see Figure 8(a). Adding Fe to any of the three starting alloys reduces $C_{Si}^{eff.}$ and hence, strength. However, the relationship deviates from the linear fit plotted in Figure 8(a), with the effect of Fe additions being worse for lower Si contents, most direful for 6060 + Fe. The non-linearity cannot be explained by the $(C_{Fe} + C_{Mn} + C_{Cr}) : C_{Si}$ ratio of 6060 + Fe: if we assume a ratio of 3 (*i.e.*, close to the measured value of 2.9, *cf.* Figure 7), $C_{Si}^{eff.}$ increases and we move even further away from the linear relationship. A more linear relationship can only be established if we assume a ratio of 1.5, but this contradicts the measured values and the Thermo-Calc calculation.

In fact, the non-linear relationship between $C_{Si}^{eff.}$ and YS is to be expected, considering that expressions for the YS increase due to shearable particles usually contain the factor $f^{1/2}$, where f is the volume fraction of hardening precipitates.[34] In other words, there are diminishing returns in terms of strength despite a linear relationship between $C_{Si}^{eff.}$ and f. In turn, however, this also means that high-Si alloys lose less strength than leaner alloys when the same absolute amount of Fe is added and thus the same absolute loss of $C_{Si}^{eff.}$ occurs.

From above analysis, it follows that compensation of Si bound in coarse intermetallic phases by additional alloying is likely to be viable, and more so the leaner the alloy. Indeed, this approach was successfully implemented in previous studies.[10–12]

However, *the more the better* is not always true. In the case of Mg and Si additions, eventually, the solubility limit of Mg_2Si and/or the Si phase will be reached, even at SHT temperature. This is another reason for the non-linearity of the strength–$C_{Si}^{eff.}$ relationship: strength

eventually plateaus at high $C_{Si}^{eff.}$. Thus, while we only consider the amount of Si lost to AlFeSi-type phases to calculate $C_{Si}^{eff.}$, the solubility limit of Mg_2Si and Si and the Mg:Si ratio (*i.e.*, whether there is enough Mg to form β''-Mg_5Si_6) must be kept in mind.

In Figure 8(b), the UTS of our alloys and several artificially aged alloys published elsewhere[10,11,14] are plotted against $C_{Si}^{eff.}$. Where data from several artificial ageing regimes was reported, the highest UTS value was taken. It can be seen that the data follows the same general trend as in this work.

According to Thermo-Calc calculations, Mg_2Si is not fully soluble in the highly alloyed variants of Wang *et al.*,[11] but some increase in strength is still visible for high $C_{Si}^{eff.}$ values.

There is a decline in strength with Fe content decreasing below 0.3 wt pct, and consequently increasing $C_{Si}^{eff.}$ in the data (alloys "#4" to "#10", "added Fe alloys") from Kato *et al.*[14] Even so, the data points are close to the overall trend, indicated by the dashed regression line. The observed local inverse trend may be

explainable by two factors: First, the amounts of Fe added were relatively low for many alloys (0.00, 0.01, 0.05, 0.10, and 0.20 wt pct for alloys "#4–#8", respectively). This means that the loss of effective Si may be offset by strengthening effects of Fe in the alloys with only minor Fe additions. Kato *et al.* Secondly, the $C0Mg$:$C_{Si}^{eff.}$ ratios of the alloys with minor Fe additions are smaller than unity (0.93–0.97 for alloys "#4–#8"), which may not be ideal for age hardening as discussed already above. This means that the age hardening potential in these alloys may not be limited by effective Si, but by available Mg.

Similarly to the values from this work, the data from Zhao *et al.*[10] clearly shows the role of effective Si. Yet, it is noticeable that the alloy with a $C_{Si}^{eff.}$ value similar to 6060 + Fe (*i.e.*, ~ 0.3 at. pct) performs much better than 6060 + Fe. It must be taken into account, however, that the alloy from Zhao *et al.* is Al–0.35Si–0.50Mg–0.20Fe (weight percentages) and thus has the same Fe content as our alloy 6060. Consequently, it appears that, while $C_{Si}^{eff.}$ is a good predictor for overall trends, the Fe content itself also plays an important role. It is conceivable, for example, that the higher number of dispersoids further reduces the age hardening potential due to interfacial segregation of Mg and Si,[35,36] although Morgeneyer *et al.*[37] found no clear evidence of such heterogeneous precipitation on dispersoids or formation of precipitate free zones around dispersoids in water-quenched material. It is also possible that 6060 + Fe could benefit from an adapted artificial ageing regime. However, Pogatscher *et al.*[38] found that an adaptation of the artificial ageing regime is not necessary for increased Fe levels when there is no significant prior natural ageing, which is the case here.

The results of Trink *et al.*,[12] who achieved remarkable improvements in mechanical properties by increasing Fe and Si levels of 6016, are not included in Figure 8(b) because the results were in T4 temper while all other results discussed here are of artificially aged tempers. Furthermore, 6016 and the alloy with increased Fe and Si levels (named 6016 + IMPs) have a much higher C_{Si}^0:C^0Mg ratio than the other alloys discussed
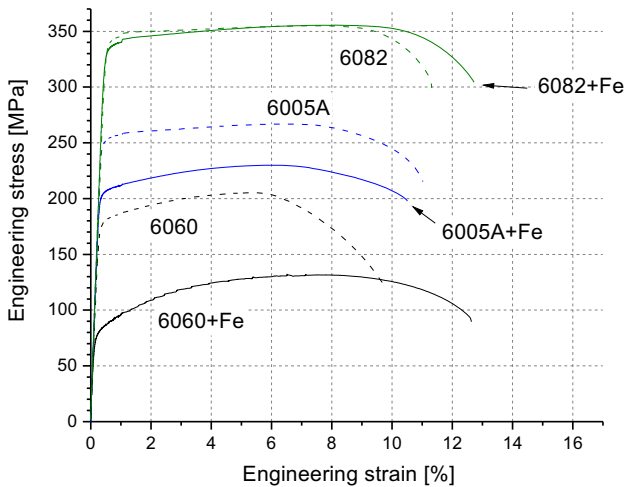

Fig. 5—Exemplary tensile curves for the six alloys after artificial ageing (8 hours, 180 °C; 2 mm/s extrusion ram speed).
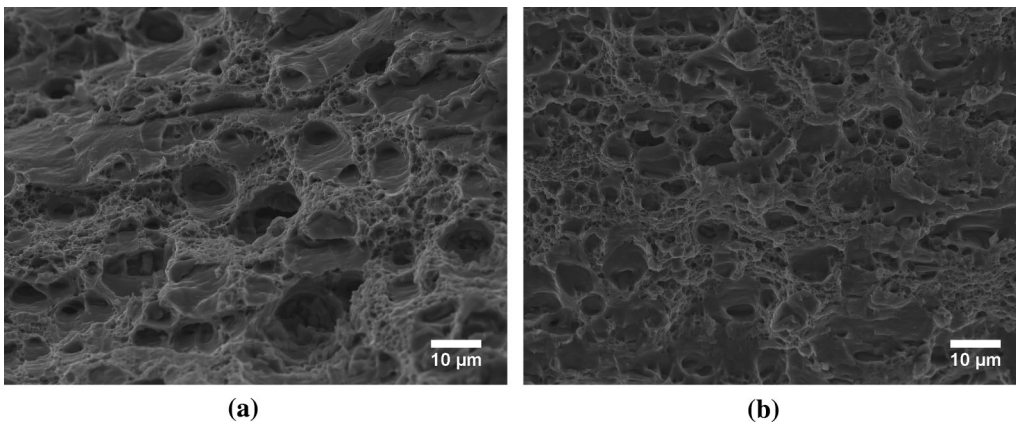

Fig. 6—Fracture surfaces of tensile specimens of 6082 (*a*) and 6082 + Fe (*b*). Combined BSE and SE micrographs.

here. Increased Si levels are known to improve T4 strength and work hardening capacity in 6016 while little influence was reported on T6 strength.[39,40] This can be explained by the consideration that the formation of the main hardening phase in artificial ageing of 6xxx, β'', is limited by Mg content rather than Si content in alloy with a high $C_{Si}^0:C^0Mg$ ratio. Trink et al.[12] achieved significantly smaller grain size than in the standard 6016 alloy and they argue that appropriate processing conditions and morphological control of the AlFeSi-type intermetallics helped to achieve surprisingly high elongation at break.

V. CONCLUSIONS

In summary, we designed 6xxx series wrought alloys with an increased, non-standard Fe content of 0.7 wt pct based on common extrusion aluminum alloys EN AW-6060, 6005A, and 6082. For comparison, versions of these alloys with a standard Fe content of 0.2 wt pct were also investigated. The amount of all other alloying elements was kept constant. After extrusion and artificial ageing, tensile testing and an in-depth analysis of the role of effective Si was performed, enriched by data points collected from the literature.

The following conclusions can be drawn:

- High strength alloys are more robust to increased Fe levels than lean alloys: 6082 + Fe achieved comparable strength to 6082 and the elongation at break is even increased. A moderate decrease in strength and comparable elongation was observed in 6005A + Fe versus 6005A; strength was still well above EN 755-2 requirements. In contrast, the addition of Fe significantly decreased the strength of 6060, resulting in mechanical properties more similar to those of unalloyed aluminum than an age-hardenable alloy.
- The main effect of Fe on strength is due to reduction of effective Si content. Effective Si is the amount of Si not bound in coarse AlFeSi-type intermetallics and thus available for age hardening.
- Given sufficient Mg content, effective Si content is a useful predictor of 6xxx series alloy strength. A $(C_{Fe} + C_{Mn} + C_{Cr}):C_{Si}$ ratio of 2 is reasonable to calculate effective Si (where C_{El} are the atomic fractions of the elements in the coarse intermetallic phases). Alternatively, CALPHAD predictions may be used.

Fig. 7—Experimentally determined $(C_{Fe} + C_{Mn} + C_{Cr}):C_{Si}$ ratio, resultant x [assuming α-Al$_{12}$(Fe, Mn, Cr)$_3$Si$_x$] of the coarse intermetallic phases (EDS/SEM) and CALPHAD prediction (Thermo-Calc). Error bars represent standard deviation of 20 point spectra per alloy.
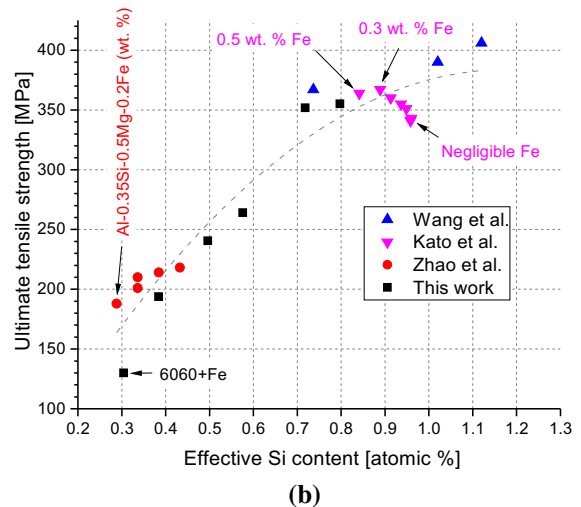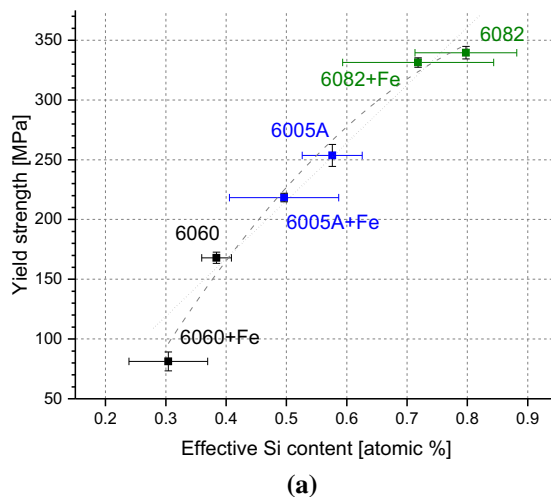

(a)

(b)

Fig. 8—(a) Yield strength after artificial ageing over effective Si content of the alloys, using Eq. [1] and $x = 1.5$. Horizontal error bars represent the ranges of effective Si content based on a possible stoichiometry of α-Al$_{12}$(Fe, Mn, Cr)$_3$Si$_x$, where $x = [1, 2]$, vertical error bars represent standard deviation of twelve measurements. (b) Ultimate tensile strength over effective Si content, with comparison to literature values. $C_{Si}^{eff.}$ calculated with Eq. [1] and $x = 1.5$ for all data points. Dotted or dashed fit lines in (a) and (b) are only a guide for the eye.

Despite the usefulness of the effective Si predictor for strength, increased Fe levels influence dispersoid formation, grain size, elongation at break, *etc*. Additional research is needed to clarify these aspects and realize the full potential of Fe-tolerant Al–Mg–Si wrought alloys.

FUNDING

CONFLICT OF INTEREST

The authors declare that they have no conflict of interest.

OPEN ACCESS

SUPPLEMENTARY INFORMATION

The online version contains supplementary material available at https://doi.org/10.1007/s11661-023-07180-z.

REFERENCES

1. J. Sarkar, T. Kutty, D. Wilkinson, J. Embury, and D. Lloyd: *Mater. Sci. Eng. A*, 2004, vol. 369, pp. 258–66.
2. J. Österreicher, A. Schiffl, G. Falkinger, and G. Bourret: *IOP Conf. Ser. Mater. Sci. Eng.*, 2016, vol. 119, p. 012028.
3. D. Lassance, D. Fabregue, F. Delannay, and T. Pardoen: *Prog. Mater. Sci.*, 2007, vol. 52, pp. 62–129.
4. M. Tokizawa, and N. Takatsuji: *Trans. Jpn Inst. Met.*, 1988, vol. 29, pp. 69–79.
5. A. Rivas, P. Munoz, S. Camero, and O. Quintero-Sayago: *Adv. Mater. Sci. Technol.*, 1999, vol. 2, pp. 15–23.
6. N. Kuijpers, F. Vermolen, C. Vuik, P. Koenis, K. Nilsen, and S. Van Der Zwaag: *Mater. Sci. Eng. A*, 2005, vol. 394, pp. 9–19.
7. F. Ostermann: *Anwendungstechnologie Aluminium*. Springer, Berlin, 2015.
8. O. Myhr, Ø. Grong, and S. Andersen: *Acta Mater.*, 2001, vol. 49, pp. 65–75.
9. D. Carron, P. Bastid, Y. Yin, and R. Faulkner: *Tech. Mech. Eur. J. Eng. Mech.*, 2010, vol. 30, pp. 29–44.
10. Q. Zhao, Z. Qian, X. Cui, Y. Wu, and X. Liu: *J. Alloys Compd.*, 2016, vol. 666, pp. 50–57.
11. Y. Wang, Y. Deng, Q. Dai, K. Jiang, J. Chen, and X. Guo: *Mater. Sci. Eng. A*, 2021, vol. 803, p. 140477.
12. B. Trink, I. Weißensteiner, P.J. Uggowitzer, K. Strobel, and S. Pogatscher: *Scripta Mater.*, 2022, vol. 215, p. 114701.
13. D. Raabe, D. Ponge, P. J. Uggowitzer, M. Roscher, M. Paolantonio, C. Liu, H. Antrekowitsch, E. Kozeschnik, D. Seidmann, B. Gault, F. De Geuser, A. Deschamps, C. Hutchinson, C. Liu, Z. Li, P. Prangnell, J. Robson, P. Shanthraj, S. Vakili, C. Sinclair, L. Bourgeois, and S. Pogatscher: *Prog. Mater. Sci.*, 2022, vol. 128, p. 100947.
14. Y. Kato, K. Hisayuki, M. Sakaguchi, and K. Higashi:: *ICAA13 Pittsburgh*, Springer, 2012, pp. 1521–26.
15. A. Arnoldt, A. Schiffl, H. Höppel, and J. Österreicher: *Mater. Charact.*, 2022, vol. 191, p. 112129.
16. *Technische Merkblätter W7 – Wärmebehandlung von Aluminium-Legierungen*. Gesamtverband der Aluminiumindustrie GDA, 2007.
17. N.C.W. Kuijpers: Kinetics of the β-AlFeSi to α-Al (FeMn) Si Transformation in Al–Mg–Si Alloys. PhD Thesis, TU Delft, 2004.
18. F. Humphreys: *Scripta Mater.*, 2000, vol. 43, p. 591–96.
19. M. Mohammadi, and H.R. Ashtiani: *Iran. J. Mater. Sci. Eng.*, 2021, vol. 18, pp. 1–17.
20. H. Rossig, G. Ibe, and W. Gruhl: *Metallurgy*, 1974, vol. 28, pp. 357–62.
21. M. Barnett, Z. Keshavarz, A. Beer, and D. Atwell: *Acta Mater.*, 2004, vol. 52, pp. 5093–5103.
22. A. Loucif, R.B. Figueiredo, T. Baudin, F. Brisset, R. Chemam, and T.G. Langdon: *Mater. Sci. Eng. A*, 2012, vol. 532, pp. 139–45.
23. J. Robson, O. Engler, C. Sigli, A. Deschamps, and W. Poole: *Metall. Mater. Trans. A*, 2020, vol. 51A, pp. 4377–89.
24. P. Goik, A. Schiffl, H. Höppel, and M. Göken: *Light Metals 2023*, Springer, 2023, pp. 568–77.
25. Y. Mahmoodkhani, J. Chen, M. Wells, W. Poole, and N. Parson: *Metall. Mater. Trans. A*, 2019, vol. 50A, pp. 5324–35.
26. J. Kronsteiner, S. Hovden, A. Arnoldt, and J. Österreicher: *Key Eng. Mater.*, 2022, vol. 926, pp. 426–35.
27. F. Grabner, J.A. Österreicher, B. Gruber, N. Papenberg, F. Gerstner, S. Kirnstötter, and C.M. Schlögl: *Adv. Eng. Mater.*, 2019, vol. 21, p. 1900089.
28. S. Andersen, H. Zandbergen, J. Jansen, C. Træholt, U. Tundal, and O. Reiso: *Acta Mater.*, 1998, vol. 46, pp. 3283–98.
29. R. Vissers, M.V. van Huis, J. Jansen, H. Zandbergen, C. Marioara, and S. Andersen: *Acta Mater.*, 2007, vol. 55, pp. 3815–23.
30. H.S. Hasting, A.G. Frøseth, S.J. Andersen, R. Vissers, J.C. Walmsley, C.D. Marioara, F. Danoix, W. Lefebvre, and R. Holmestad: *J. Appl. Phys.*, 2009, vol. 106, p. 123527.
31. S.J. Andersen, C.D. Marioara, J. Friis, S. Wenner, and R. Holmestad: *Adv. Phys. X*, 2018, vol. 3, p. 1479984.
32. G. Edwards, K. Stiller, G. Dunlop, and M. Couper: *Acta Mater.*, 1998, vol. 46, pp. 3893–3904.
33. E. Kovács-Csetényi, C. Vassel, and I. Kovacs: *Phys. Status Solidi B*, 1966, vol. 17, pp. K123–26.
34. T. Gladman: *Mater. Sci. Technol.*, 1999, vol. 15, pp. 30–36.
35. K. Strobel, M.A. Easton, L. Sweet, M.J. Couper, and J.-F. Nie: *Mater. Trans.*, 2011, vol. 52, pp. 914–19.
36. J. Famelton, G. Hughes, C. Williams, C. Barbatti, M. Moody, and P. Bagot: *Mater. Charact.*, 2021, vol. 178, p. 111194.
37. T. Morgeneyer, M. Starink, S. Wang, and I. Sinclair: *Acta Mater.*, 2008, vol. 56, pp. 2872–84.
38. S. Pogatscher, H. Antrekowitsch, and P.J. Uggowitzer: *Acta Mater.*, 2012, vol. 60, pp. 5545–54.
39. S. Hirth, G. Marshall, S. Court, and D. Lloyd: *Mater. Sci. Eng. A*, 2001, vol. 319, pp. 452–56.
40. H. Zhong, P.A. Rometsch, L. Cao, and Y. Estrin: *Mater. Sci. Eng. A*, 2016, vol. 651, pp. 688–97.